Hybrid Lattice Boltzmann/Finite Difference simulations of viscoelastic multicomponent flows in confined geometries

A. Gupta[1], M. Sbragaglia[1], A: Scagliarini[1]

[1] Department of Physics and INFN, University of "Tor Vergata", Via della Ricerca Scientifica 1, 00133 Rome, Italy

Abstract

We propose numerical simulations of viscoelastic fluids based on a hybrid algorithm combining Lattice-Boltzmann models (LBM) and Finite Differences (FD) schemes, the former used to model the macroscopic hydrodynamic equations, and the latter used to model the polymer dynamics. The kinetics of the polymers is introduced using constitutive equations for viscoelastic fluids with finitely extensible non-linear elastic dumbbells with Peterlin's closure (FENE-P). The numerical model is first benchmarked by characterizing the rheological behaviour of dilute homogeneous solutions in various configurations, including steady shear, elongational flows, transient shear and oscillatory flows. As an upgrade of complexity, we study the model in presence of non-ideal multicomponent interfaces, where immiscibility is introduced in the LBM description using the "Shan-Chen" model. The problem of a confined viscoelastic (Newtonian) droplet in a Newtonian (viscoelastic) matrix under simple shear is investigated and numerical results are compared with the predictions of various theoretical models. The proposed numerical simulations explore problems where the capabilities of LBM were never quantified before.

I. INTRODUCTION

Lattice Boltzmann methods (LBM) are nowdays recognized as powerful computational tools for the simulation of hydrodynamic phenomena [1–6]. Historically, the main successful applications in the context of computational fluid dynamics pertain the weakly compressible Navier-Stokes equations [1–4] and models associated with more complex flows involving phase transition/separation [7, 8]. However, the spectrum of applications and strengths of LBM in simulating new challenging problems keeps on expanding [6, 9–14]. The LBM does not solve directly the hydrodynamic conservation equations, but rather models the streaming and collision (i.e. relaxation towards local equilibria) of particles, thus offering a series of advantages [1–6]. In this paper, we apply the LBM to the simulation of multicomponent viscoelastic fluids. Emulsions or polymer melts, which are present in many industrial and everyday life products, are good examples of such fluids, having the relevant constituents a viscoelastic -rather than a Newtonian- nature [15]. We will introduce the kinetics of the polymers using constitutive equations for finitely extensible non-linear elastic dumbbells with Peterlin's closure (FENE-P) [16, 17], in which the dumbbells can only be stretched by a finite amount, the latter effect parametrized with a maximum extensional length squared L^2. The model supports a positive first normal stress difference and a zero second normal stress difference in steady shear. It also supports a thinning effect at large shear, which disappears when $L^2 \gg 1$, a limit where we recover the so-called Oldroyd-B model [18]. Both the FENE-P and Oldroyd-B models have been investigated in many details with other methods based on finite differences [19, 20], finite volumes [21], diffuse interface models [22, 23], finite elements [24] and spectral element methods [25]. There have been already various attempts done with LBM in this direction too. Qian & Deng [26] proposed a modification of the equilibrium distribution to account for the elastic effects, whereas in Ispolatov and Grant [27] the elastic effects are taken into account within the framework of a Maxwell model. In Giraud *et al.* [28, 29] and in Lallemand *et al.* [30] LBM schemes for solving the Jeffreys model were proposed, with the hydrodynamic behavior of the LBM emerging with memory effects. In a recent paper, Malaspinas *et al.* [31] proposed a new approach to simulate linear and non-linear viscoelastic fluids and in particular those described by the Oldroyd-B and FENE-P constitutive equations. The authors studied and benchmarked the model against various problems, including the 3D Taylor-Green vortex decay, the simplified 2D four-rolls mill, and the 2D Poiseuille flow. A similar approach was used by Denniston et al. [32] and Marenduzzo et al. [33] for the simulation of flows of liquid crystals.

2

In other works by Onishi *et al.* [34, 35], the Fokker-Plank counterpart for the Oldroyd-B and FENE-P models was introduced to carry out simulations with the help of the LBM. The numerical results presented explored the problem of droplet deformation under steady shear. A formulation based on the Fokker-Planck equation was also recently studied by Ansumali & coworkers [36]: the approach was benchmarked by determining the bulk rheological properties for both steady and time-dependent shear and extensional flows, from moderate to large Weissenberg numbers. Finally, we also remark that due to the efficiency of LBM solvers, the latter have been used to replace macroscopic flow solvers for describing dilute polymer solutions [37].

As witnessed by an increasing amount of works (see [6] and references therein), LBM has been proven to be particularly suitable to the study of multicomponent systems where interfacial dynamics and phase separation are present, since it can capture basic essential features, even with simplified kinetic models. Significant progress has recently been made in this direction, as evidenced by many LBM that have been developed on the basis of different points of view, including the Gunstensen model [38, 39], the "Shan-Chen" model [7, 8, 40], the free-energy model [41]. However, investigations of viscoelastic flows within the framework of non-ideal multicomponent LBM are rare. The work that better fits these requirements is probably the one by Onishi *et al.* [34, 35], but the problems there presented suffer of scarce exploration of the effects of confinement and structure of the flow [42–47]. Here we go a step forward by presenting a comprehensive study related to the characterization of viscoelastic effects for multicomponent LBM in confined geometries. We numerically and theoretically explore the potentiality of a coupled approach, based on LBM and Finite Difference (FD) schemes, the former used to model two immiscible fluids with variable viscous ratio, and the latter used to model the polymer dynamics. The numerical model is first benchmarked without phase separation, by characterizing the rheological behaviour of dilute homogeneous solutions with FENE-P model in various steady states (shear and elongational) and transient flows. As an upgrade of complexity, we study the model in presence of non-ideal multicomponent interfaces, where immiscibility is introduced in the LBM description using the "Shan-Chen" model [7, 8, 40, 48]. The problem of a confined viscoelastic (Newtonian) droplet in a Newtonian (viscoelastic) matrix under steady shear is investigated and numerical results are compared with the prediction of various theoretical models.

II. COMPUTATIONAL MODEL

In this section we report the essential technical details of the numerical scheme used. We refer the interested reader to the reference papers [7, 8, 19, 40, 49–52], where all the details can be found. We consider the Navier-Stokes (NS) and FENE-P reference equations for a binary mixture of two components (A, B) in the following form:

$$\partial_t \rho_\sigma + \boldsymbol{\nabla} \cdot (\rho_\sigma \boldsymbol{u}) = \boldsymbol{\nabla} \cdot \boldsymbol{D}_{S,\sigma}; \qquad \sigma = A, B \tag{1}$$

$$\rho \left[\partial_t \boldsymbol{u} + (\boldsymbol{u} \cdot \boldsymbol{\nabla}) \boldsymbol{u} \right] = -\boldsymbol{\nabla} p + \boldsymbol{\nabla} \cdot \boldsymbol{\sigma}_S + \frac{\eta_P}{\tau_P} \boldsymbol{\nabla} \cdot \boldsymbol{\sigma}_P + \sum_\sigma \boldsymbol{g}_\sigma; \tag{2}$$

$$\partial_t \mathscr{C} + (\boldsymbol{u} \cdot \boldsymbol{\nabla}) \mathscr{C} = \mathscr{C} \cdot (\boldsymbol{\nabla} \boldsymbol{u}) + (\boldsymbol{\nabla} \boldsymbol{u})^T \cdot \mathscr{C} - \frac{\boldsymbol{\sigma}_P - 1}{\tau_P}. \tag{3}$$

Here, ρ_σ is the density of the σ-th component ($\rho = \sum_\sigma \rho_\sigma$ indicates the total density), $\boldsymbol{u}$ represents the baricentric velocity of the mixture, and $p_\sigma = c_s^2 \rho_\sigma$ is the internal ideal pressure of component σ, with $p = \sum_\sigma p_\sigma$. The diffusion current of one component into the other and the viscous stress tensor of the solvent (S) fluid are

$$\boldsymbol{D}_{S,\sigma} = \mu \left[\left(\boldsymbol{\nabla} p_\sigma - \frac{\rho_\sigma}{\rho} \boldsymbol{\nabla} p \right) - \left(\boldsymbol{g}_\sigma - \frac{\rho_\sigma}{\rho} \sum_\sigma \boldsymbol{g}_\sigma \right) \right] \tag{4}$$

$$\boldsymbol{\sigma}_S = \eta_s \left(\boldsymbol{\nabla} \boldsymbol{u} + (\boldsymbol{\nabla} \boldsymbol{u})^T - \frac{2}{3} \mathbf{1} (\boldsymbol{\nabla} \cdot \boldsymbol{u}) \right) + \eta_b \mathbf{1} (\boldsymbol{\nabla} \cdot \boldsymbol{u}). \tag{5}$$

The viscosity coefficients are the shear viscosity η_s and the bulk viscosity η_b, while the coefficient μ is a mobility parameter regulating the intensity of the diffusion. The term $\sum_\sigma \boldsymbol{g}_\sigma$ in equation (2) refers to all the contributions coming from internal and external forces. As for the internal forces, we will use the "Shan-Chen" model [7] for multicomponent mixtures. The force experienced by the particles of the σ-th species at $\boldsymbol{x}$, is due to the particles of the other species at the neighbouring locations

$$\boldsymbol{g}_\sigma(\boldsymbol{x}) = -\mathscr{G} \rho_\sigma(\boldsymbol{x}) \sum_\alpha \sum_{\sigma' \neq \sigma} w_\alpha \rho_{\sigma'}(\boldsymbol{x} + \boldsymbol{c}_\alpha) \boldsymbol{c}_\alpha \qquad \sigma, \sigma' = A, B \tag{6}$$

where $\mathscr{G}$ is a parameter that regulates the interactions between the two components. The sum in equation (6) extends over a set of interaction links $\boldsymbol{c}_\alpha$ coinciding with those of the LBM dynamics (see below). When the coupling strength parameter $\mathscr{G}$ is sufficiently large, demixing occurs and the model can describe stable interfaces with a surface tension. The effect of the internal forces can be recast into the gradient of the pressure tensor $\boldsymbol{P}^{(int)}$ [48], thus modifying the internal pressure

of the model, i.e. $\boldsymbol{P} = p\mathbf{1} + \boldsymbol{P}^{(int)}$, with

$$\boldsymbol{P}^{(int)}(\boldsymbol{x}) = -\frac{1}{2}\mathscr{G}\rho_A(\boldsymbol{x})\sum_\alpha w_\alpha \rho_B(\boldsymbol{x}+\boldsymbol{c}_\alpha)\boldsymbol{c}_\alpha\boldsymbol{c}_\alpha - \frac{1}{2}\mathscr{G}\rho_B(\boldsymbol{x})\sum_\alpha w_\alpha \rho_A(\boldsymbol{x}+\boldsymbol{c}_\alpha)\boldsymbol{c}_\alpha\boldsymbol{c}_\alpha. \quad (7)$$

Upon Taylor expanding the expression (7), we get a pressure contribution in the bulk pressure $P_b = p + c_s^2 \mathscr{G}\rho_A\rho_B$ and other contributions which are proportional to the derivatives of both densities. The latter contributions are responsible for the surface tension at the non ideal interface [40]. A proper tuning of the density gradients in contact with the wall allows for the modelling the wetting properties. In all the simulations described in this paper, the resulting contact angle for a droplet placed in contact with the solid walls is $\theta_{eq} = 90°$ (i.e. neutral wetting).

As for the polymer details in equations (2) and (3), $\mathscr{C} \equiv \langle \mathscr{R}_i \mathscr{R}_j \rangle$ is the polymer-conformation tensor, i.e. the ensemble average of the tensor product of the end-to-end distance vector $\mathscr{R}_i$, which equals the identity tensor ($\mathscr{C} = \mathbf{1}$) at equilibrium, η_P is the viscosity parameter for the FENE-P solute and τ_P the polymer relaxation time. The polymer feedback into the fluid is parametrized by $\frac{\eta_P}{\tau_P}\boldsymbol{\sigma}_P = \frac{\eta_P}{\tau_P}f(r_P)\mathscr{C}$, being $\boldsymbol{\sigma}_P = f(r_P)\mathscr{C}$ the dimensionless counterpart. The FENE-P potential is encoded in $f(r_P) \equiv (L^2-3)/(L^2-r_P^2)$, which ensures finite extensibility, $r_P \equiv \sqrt{Tr(\mathscr{C})}$ and L are the trace and the (dimensionless) maximum possible extension, respectively, of the polymers [17]. As L decreases, the polymer dumbbell becomes less extensible and the maximum level of stress attainable is reduced. In a homogeneous steady uniaxial extension, the extensional viscosity of the polymers increases proportionally to the maximum dumbbell length squared and it becomes infinite in the limit $L^2 \gg 1$ [18] (see subsection (III B)).

The fluid part of the model (equation (2)) is obtained from a LBM featuring a multiple relaxation time scheme (MRT). Further technical details of the algorithm can be found in [49–51], here we just report the essential features of the model. The LBM equation considers the probability density function, $f_\alpha^{(\sigma)}(\boldsymbol{x},t)$, to find a particle of component σ in the space-time location $(\boldsymbol{x},t)$ with discrete velocity $\boldsymbol{c}_\alpha$. In a unitary time lapse, the evolution equation for $f_\alpha^{(\sigma)}(\boldsymbol{x},t)$ is (double indexes are meant summed upon)

$$f_\alpha^{(\sigma)}(\boldsymbol{x}+\boldsymbol{c}_\alpha,t+1) - f_\alpha^{(\sigma)}(\boldsymbol{x},t) = -\Lambda_{\alpha\beta}\left(f_\beta^{(\sigma)} - E_\beta^{(\sigma)}(\rho_\sigma,\boldsymbol{u})\right) + \left(I_{\alpha\beta} - \frac{1}{2}\Lambda_{\alpha\beta}\right)S_\beta(\boldsymbol{u},\boldsymbol{g}_\sigma). \quad (8)$$

The equilibrium functions are chosen to be

$$E_\alpha^{(\sigma)}(\rho,\boldsymbol{u}) = w_\alpha\rho\left[1 + \frac{\boldsymbol{c}_\alpha \cdot \boldsymbol{u}}{c_s^2} + \frac{\boldsymbol{u}\boldsymbol{u} : (\boldsymbol{c}_\alpha\boldsymbol{c}_\alpha - c_s^2\mathbf{1})}{2c_s^4}\right] \quad (9)$$

5

where $c_s^2 = 1/3$ is a constant in the model and the weights w_α for the D3Q19 [49] LBM used are

$$w_\alpha = \begin{cases} \frac{1}{3} & \alpha = 0 \\ \frac{1}{18} & \alpha = 1 - 6 \\ \frac{1}{36} & \alpha = 7 - 18. \end{cases} \tag{10}$$

The relaxation towards equilibrium is regulated by the matrix $\Lambda_{\alpha\beta}$, the same for both species. The source term $S_\alpha(\boldsymbol{u}, \boldsymbol{g}_\sigma)$ is chosen as

$$S_\alpha(\boldsymbol{u}, \boldsymbol{g}_\sigma) = w_\alpha \left[\frac{(\boldsymbol{c}_\alpha - \boldsymbol{u})}{c_s^2} + \frac{(\boldsymbol{c}_\alpha \cdot \boldsymbol{u})}{c_s^4} \boldsymbol{c}_\alpha \right] \cdot \boldsymbol{g}_\sigma \tag{11}$$

and the macroscopic variables are the hydrodynamical density (one for each specie) and the common fluid velocity

$$\rho_\sigma(\boldsymbol{x}, t) = \sum_{\alpha=0}^{18} f_\alpha^{(\sigma)}(\boldsymbol{x}, t) \quad \rho \tilde{\boldsymbol{u}}(\boldsymbol{x}, t) = \sum_\sigma \sum_{\alpha=0}^{18} \boldsymbol{c}_\alpha f_\alpha^{(\sigma)}(\boldsymbol{x}, t). \tag{12}$$

We also choose the equilibrium velocity as the velocity of the whole fluid plus half of the total forcing contribution, i.e. the standard way to define the hydrodynamical velocity in the lattice Boltzmann scheme [3, 40]

$$\boldsymbol{u}(\boldsymbol{x}, t) = \tilde{\boldsymbol{u}}(\boldsymbol{x}, t) + \frac{\sum_\sigma \boldsymbol{g}_\sigma}{2\rho}. \tag{13}$$

In order to perform the relaxation process towards equilibrium, in the spirit of the MRT models, we need to construct sets of linearly independent moments from the distribution functions in velocity space. The moments are constructed from the distribution function through a transformation matrix $\mathscr{T}$ comprising a linearly independent set of vectors, i.e. $\hat{\boldsymbol{f}}^{(\sigma)} = \mathscr{T} \boldsymbol{f}^{(\sigma)}$, with the transformation matrix $\mathscr{T}$ suitably constructed in terms of the velocity links [49–51]. In the moments space, the collisional operator $\Lambda_{\alpha\beta}$ in the lattice Boltzmann equation (8) is diagonal, thus offering the particular advantage to relax the various processes (diffusive processes and viscous processes) independently. The relaxation times of the momentum (τ_M), bulk (τ_b) and shear (τ_s) modes in (8) are indeed related to the transport coefficients of hydrodynamics as

$$\mu = \left(\tau_M - \frac{1}{2} \right) \quad \eta_s = \rho c_s^2 \left(\tau_s - \frac{1}{2} \right) \quad \eta_b = \frac{2}{3} \rho c_s^2 \left(\tau_b - \frac{1}{2} \right). \tag{14}$$

Some of the modes ($\Pi_\sigma^{(eq)}$) of the equilibrium distribution functions $E_\alpha^{(\sigma)}(\rho_\sigma, \boldsymbol{u})$ are explicitly affected by the second order tensor of the distribution, i.e. $\sum_\alpha f_\alpha^{(\sigma)} \boldsymbol{c}_\alpha \boldsymbol{c}_\alpha$. The polymer stress $\frac{\eta_P}{\tau_P} \boldsymbol{\sigma}_P = \frac{\eta_P}{\tau_P} f(r_P) \mathscr{C}$ appearing in equation (3) is then added to these modes with a weight that depends on the species, i.e.

$$\Pi_\sigma^{(eq)} = \Pi_\sigma^{(eq)} - \frac{\rho_\sigma}{\rho} \frac{\eta_P}{\tau_P} f(r_P) \mathscr{C}. \tag{15}$$

6

The recovery of the hydrodynamical limit described by equations (1-2) is ensured by the Chapman-Enskog analysis [2, 3]. Repeating the calculations reported in [49], a contribution coming from the polymer stress is found to affect the viscous stress of the equations. Such contribution is measured to be rather small in all the numerical simulations done, ensuring that the balance equations (1-3) are reproduced in our simulations. In particular, the weight function ρ_σ/ρ ensures that the global momentum balance equation (2) has the total stress $\frac{\eta_P}{\tau_P}f(r_P)\mathscr{C}$ in the rhs. The idea of changing the lattice Boltzmann stress with a contribution directly related to the polymers feedback stress echoes the work Onishi *et al.* [34, 35], although the authors used a simple single relaxation time scheme. The relaxation frequencies in (14) are chosen in such a way that $\tau_M = 1.0$ lbu (lattice Boltzmann units) and $\tau_s = \tau_b$, corresponding to a bulk viscosity equal to the shear viscosity, $\eta_s = \eta_b$ in equation (5). The viscous ratio of the Lattice Boltzmann fluid is changed by letting τ_s depend on space

$$\rho c_s^2 \left(\tau_s - \frac{1}{2} \right) = \eta_s = \eta_A f_+(\phi) + \eta_B f_-(\phi) \tag{16}$$

where $\phi = \phi(x) = \frac{\rho_A(x)-\rho_B(x)}{\rho_A(x)+\rho_B(x)}$ represents the order parameter. We have indicated with $\eta_{A,B}$ the bulk viscosities in the regions with a majority of one of the two components (*A* or *B*). The functions $f_\pm(\phi)$ are chosen as

$$f_\pm(\phi) = \left(\frac{1 \pm \tanh(\phi/\Delta)}{2} \right). \tag{17}$$

The smoothing parameter $\Delta = 0.1$ is chosen sufficiently small so as to recover a matching with analytical predictions for droplet deformation and orientation in shear flow.

As for the polymer constitutive equation, we are following the two References [19, 52] to solve the FENE-P equation (3): we use an explicit second-order central-finite-difference scheme in space and a second-order Adams-Bashforth method for temporal evolution. We maintain the symmetric-positive-definite (SPD) nature of conformation tensor at all times by using the Cholesky-decomposition scheme [52]. We first consider the equation for $\boldsymbol{\sigma}_P = f(r_P)\mathscr{C}$. Since $\mathscr{C}$ and hence $\boldsymbol{\sigma}_P$ are SPD matrices, we can write $\boldsymbol{\sigma}_P = \mathscr{L}\mathscr{L}^T$, where $\mathscr{L}$ is a lower-triangular matrix with elements $\ell_{ij} = 0$ if $j > i$. Thus, the equation for $\boldsymbol{\sigma}_P$ yields an equation set that ensures the SPD of $\mathscr{C}$ if $\ell_{ii} > 0$ [52], a condition which we enforce explicitly by considering the evolution of $\ln \ell_{ii}$ instead of ℓ_{ii} [19]. As for the boundary condition for the conformation tensor $\mathscr{C}$, we use linear extrapolation at the boundaries.

Finally, in order to study separately the effects of matrix and droplet viscoelasticity, we follow the methodologies already developed by Yue *et al.* [22], by allowing the feedback in equation (2) to

be modulated in space with the functions $f_\pm(\phi)$

$$\rho\left[\partial_t \boldsymbol{u} + (\boldsymbol{u} \cdot \boldsymbol{\nabla})\boldsymbol{u}\right] = -\boldsymbol{\nabla}P + \boldsymbol{\nabla}\left[(\eta_A f_+(\phi) + \eta_B f_-(\phi))(\boldsymbol{\nabla}\boldsymbol{u} + (\boldsymbol{\nabla}\boldsymbol{u})^T)\right] + \frac{\eta_P}{\tau_P}\boldsymbol{\nabla}[f(r_P)\mathscr{C}f_\pm(\phi)].$$

(18)

We remark that other possibilities already exist for implementing the polymer dynamics in LBM [31, 34–36], either by considering directly the evolution equation (3) [31], or considering the the Fokker-Plank counterpart [34–36]. Our algorithm is surely curing problems related to the polymer extension and conformation tensor, which have to remain bounded and positive definite at all times, respectively, for the calculation to remain stable. Nevertheless, we stress that it is not the aim of this paper to propose a comparative study with respect to other existing LBM (or closely related) approaches, as we are interested in assessing the robustness of the methodology in simulating confined problems with multicomponent phases and viscoelastic nature.

III.   HOMOGENEOUS DILUTE SUSPENSIONS: RHEOLOGY

In order to validate the numerical scheme described in section (II), we examined the bulk rheological properties in some canonical steady flow situations, i.e. simple shear flow (section III A) and extensional flow (section III B), and also benchmarked time-dependent situations, by verifying the linear viscoelastic behaviour in a small-amplitude oscillatory shearing (section III C) and the stress relaxation after cessation of a shear flow (section III D) [53, 54]. To do that, we switch to zero the coupling constant $\mathscr{G}$ in equation (6), thereby reducing to the case of two miscible gases with an ideal equation of state. In addition, we will work with load conditions ensuring very weak compressibility of the system.

To properly establish a link between the evolution equation of the conformation tensor (3) and known results published in the literature [53, 54], we prefer to rewrite the equation for the polymer feedback stress. Starting from the dimensionless polymer feedback stress

$$\boldsymbol{\sigma}_P = f(r_P)\mathscr{C} = \frac{(L^2 - 3)}{(L^2 - Tr(\mathscr{C}))}\mathscr{C}$$

(19)

and taking the trace of equation (19), we find $Tr(\mathscr{C}) = \frac{L^2 Tr(\boldsymbol{\sigma}_P)}{L^2 - 3 + Tr(\boldsymbol{\sigma}_P)}$ and the feedback (19) can be rewritten as

$$\boldsymbol{\sigma}_P = \frac{(L^2 - 3)}{(L^2 - \frac{L^2 Tr(\boldsymbol{\sigma}_P)}{L^2 - 3 + Tr(\boldsymbol{\sigma}_P)})}\mathscr{C} = \frac{L^2 - 3 + Tr(\boldsymbol{\sigma}_P)}{L^2}\mathscr{C} = Z(Tr(\boldsymbol{\sigma}_P))\mathscr{C}$$

(20)

8

where we have defined $Z(Tr(\boldsymbol{\sigma}_P)) = \frac{L^2 - 3 + Tr(\boldsymbol{\sigma}_P)}{L^2}$. The equation of the conformation tensor (3), with the substitution $\mathscr{C} = \boldsymbol{\sigma}_P/Z$, becomes

$$\tau_P \left[\frac{1}{Z} D_t \boldsymbol{\sigma}_P - \frac{1}{Z} \boldsymbol{\sigma}_P \cdot (\boldsymbol{\nabla} \boldsymbol{u}) - \frac{1}{Z} (\boldsymbol{\nabla} \boldsymbol{u})^T \cdot \boldsymbol{\sigma}_P - \frac{\boldsymbol{\sigma}_P}{Z^2} D_t Z \right] = -\boldsymbol{\sigma}_P + \mathbf{1} \tag{21}$$

or equivalently

$$Z(\boldsymbol{\sigma}_P - \mathbf{1}) + \tau_P \left[D_t \boldsymbol{\sigma}_P - \boldsymbol{\sigma}_P \cdot (\boldsymbol{\nabla} \boldsymbol{u}) - (\boldsymbol{\nabla} \boldsymbol{u})^T \cdot \boldsymbol{\sigma}_P - \boldsymbol{\sigma}_P D_t \log Z \right] = 0 \tag{22}$$

which directly maps into the equation considered by Bird *et al.* [53] (their equation (10) and subsequent developments). In the following sections we provide benchmark tests for various situations. All the analytical results used can be found in other papers [17, 53–55] and we limit ourself to a brief review for the sake of completeness.

A. Steady Shear Flow

We consider equation (22) under the effect of a homogeneous shear flow, $u_x = \dot{\gamma} y$, $u_y = 0$, $u_z = 0$, in equations (22). The equations, written out in components, become

$$Z \begin{pmatrix} \sigma_{P,xx} - 1 & \sigma_{P,xy} & 0 \\ \sigma_{P,yx} & \sigma_{P,yy} - 1 & 0 \\ 0 & 0 & \sigma_{P,zz} - 1 \end{pmatrix} - \tau_P \left[\dot{\gamma} \begin{pmatrix} 2\sigma_{P,yx} & \sigma_{P,yy} & 0 \\ \sigma_{P,yy} & 0 & 0 \\ 0 & 0 & 0 \end{pmatrix} \right] = 0. \tag{23}$$

We find $\sigma_{P,yy} = \sigma_{P,zz} = 1$ so that $Z = \frac{L^2 - 1 + \sigma_{P,xx}}{L^2}$. The xx and xy components of equation (23) reduce to the system

$$\begin{cases} \left(1 + \frac{N}{L^2}\right) N = 2\Lambda S \\ \left(1 + \frac{N}{L^2}\right) S = \Lambda \end{cases} \tag{24}$$

where $N = (\sigma_{P,xx} - 1)$, $\Lambda = \tau_P \dot{\gamma}$, $S = \sigma_{P,xy}$. The quantities N and S represent the first *normal stress difference* and the polymer shear Stress [17, 53] developing in steady shear, respectively. The first normal stress difference is a typical signature of viscoelasticity [17], while from the polymer shear stress we can extract (by dividing for the shear rate) the polymer contribution to the shear viscosity. We immediately see from equations (24) that the first normal stress difference hinges on the knowledge of the polymer shear stress

$$N = 2S^2 \tag{25}$$

9

with S satisfying the following equation

$$2\frac{S^3}{L^2} + S - \Lambda = 0. \tag{26}$$

This equation can be solved exactly [17, 53, 55]

$$S(\Lambda, L) = 2\left(\frac{L^2}{6}\right)^{1/2} \sinh\left(\frac{1}{3}\text{arcsinh}\left(\frac{\Lambda L^2}{4}\left(\frac{L^2}{6}\right)^{-3/2}\right)\right) \tag{27}$$

and, from equation (25) we find N as

$$N(\Lambda, L) = 8\left(\frac{L^2}{6}\right) \sinh^2\left(\frac{1}{3}\text{arcsinh}\left(\frac{\Lambda L^2}{4}\left(\frac{L^2}{6}\right)^{-3/2}\right)\right) \tag{28}$$

Going back to equation (2), we see that the polymer shear stress $\frac{\eta_P}{\tau_P}\sigma_{P,xy} = \frac{\eta_P}{\tau_P}S$ produces a constant shear viscosity only in the Oldroyd-B limit ($S \approx \Lambda = \dot{\gamma}\tau_P$ as $L^2 \gg 1$), while thinning effects are present for finite values of L^2.

In figure 1 we present numerical simulations to benchmark these results. The numerical simulations have been carried out in three dimensional domains with $L_x \times H \times L_z = 2 \times 60 \times 2$ cells. Periodic conditions are applied in the stream-flow (x) and in the transverse-flow (z) directions. The linear shear flow $u_x = \dot{\gamma}y$, $u_y = u_z = 0$ is imposed in the LBM scheme by applying two opposite velocities in the stream-flow direction ($u_x(x, y = 0, z) = -u_x(x, y = H, z) = U_w$) at the upper ($y = H$) and lower wall ($y = 0$) with the bounce-back rule [3]. We next change the shear in the range $10^{-6} \leq 2U_w/H \leq 10^{-2}$ lbu and the polymer relaxation time in the range $10^3 \leq \tau_P \leq 10^5$ lbu for two values of the finite extensibility parameter, $L^2 = 10^2, 10^4$, and fixed $\eta_P = 0.136$ lbu. In figure 1 we report the first normal stress difference (left panel) and the dimensionless polymer shear viscosity (right panel), both rescaled with the polymer viscosity η_P, as a function of the dimensionless shear $\Lambda = \tau_P\dot{\gamma}$. The values of the conformation tensor are taken when the simulation has reached the steady state. All the numerical simulations collapse on different master curves, dependently on the value of L^2. The normal stress difference N increases at large Λ to exhibit variable levels depending on L^2, and consistently with the theoretical prediction of equation (28). The dependence of the normal stress N from L^2 directly reflects in the presence of thinning effects visible in the plot of the polymer shear viscosity (see right panel of figure 1).
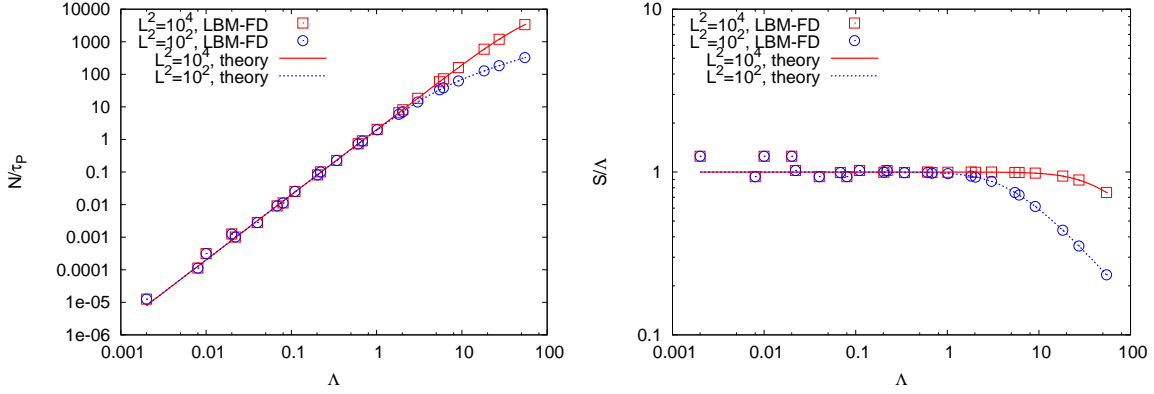
FIG. 1: We plot the first normal stress difference and the polymer shear viscosity (both scaled with the polymer viscosity η_P) as a function of the dimensionless shear $\Lambda = \tau_P \dot{\gamma}$. Symbols are the results of the LBM-FD simulations with different imposed shears, different τ_P and different L^2 (see text for details). All the numerical simulations collapse on different master curves, dependently on the value of L^2: $L^2 = 10^2$ (circles) and $L^2 = 10^4$ (squares). The lines are the theoretical predictions based on equations (27) and (28).

B. Steady Elongational Flow

We consider equation (22) under the effect of a steady elongational flow, $u_z = \dot{\varepsilon}z$, $u_x = -\dot{\varepsilon}x/2$, $u_y = -\dot{\varepsilon}y/2$, with $\dot{\varepsilon}$ the elongation rate. Again, writing out all the components we get

$$Z \begin{pmatrix} \sigma_{P,xx} - 1 & 0 & 0 \\ 0 & \sigma_{P,yy} - 1 & 0 \\ 0 & 0 & \sigma_{P,zz} - 1 \end{pmatrix} + \tau_P \left[\dot{\varepsilon} \begin{pmatrix} \sigma_{P,xx} & 0 & 0 \\ 0 & \sigma_{P,yy} & 0 \\ 0 & 0 & -2\sigma_{P,zz} \end{pmatrix} \right] = 0 \qquad (29)$$

implying $\sigma_{P,xx} = \sigma_{P,yy}$. By denoting with $T = Tr(\sigma_P) - 3$ and $D = \sigma_{P,zz} - \sigma_{P,xx}$. After defining the dimensionless elongation rate $\Lambda_e = \tau_P \dot{\varepsilon}$, we find two independent equations for T and D

$$\begin{cases} \dfrac{L^2 + T}{L^2} T - 2\Lambda_e D = 0 \\ -\dfrac{L^2 + T}{L^2} D + \Lambda_e (D + T) + 3\Lambda_e = 0 \end{cases} \qquad (30)$$

which can be rearranged to give us a cubic equation for D as a function of Λ_e. Such equation is most conveniently written as a quadratic equation in Λ_e:

$$2L^2 D \Lambda_e^2 + \left[-4D^2 + (L^2 - D - 3)(D + 3) \right] \Lambda_e + \frac{2D^3}{L^2} - (L^2 - D - 3)D = 0 \qquad (31)$$

with associated solutions

$$(\Lambda_e)_{+,-} = \frac{-P_2 \pm \sqrt{P_2^2 - 4P_1 P_3}}{2P_1} \qquad (32)$$

11

where

$$\begin{cases} P_1 = 2DL^2 \\ P_2 = -4D^2 + (L^2 - D - 3)(D + 3) \\ P_3 = \frac{2D^3}{L^2} - (L^2 - D - 3)D. \end{cases} \quad (33)$$

The *elongational* viscosity

$$\eta_e = \frac{\eta_P}{\tau_P} \frac{D}{\dot{\varepsilon}} \quad (34)$$

can be computed by numerically inverting equations (32-33) and paying attention to a proper selection of the sign in equation (32). For small D the solution is given by $(\Lambda_e)_+$, as $(\Lambda_e)_-$ is negative and divergent. The asymptotic expansion for small D is indeed given by

$$(\Lambda_e)_+ = \frac{-P_2 + \sqrt{P_2^2 - 4P_1 P_3}}{2P_1} \approx \frac{D}{3} + \mathcal{O}(D^2) \quad (35)$$

showing that the elongational viscosity approaches a constant value at low elongation rates, which is three times the corresponding zero-shear-rate viscosity. However the radicand of equation (32) is zero when $D = L^2 - 3$. In such a point, in order to preserve the continuity of the derivative of Λ_e, we need to consider $(\Lambda_e)_-$ as a solution. Consistently, for large D, we find

$$(\Lambda_e)_- = \frac{-P_2 - \sqrt{P_2^2 - 4P_1 P_3}}{2P_1} \approx \frac{D}{2L^2} + \mathcal{O}\left(\frac{1}{D}\right). \quad (36)$$

We therefore find the following asymptotic expansion for the elongational viscosity

$$\frac{\eta_e}{\eta_P} = \frac{1}{\tau_P} \frac{D}{\dot{\varepsilon}} = \begin{cases} 3 & \dot{\varepsilon} \ll 1 \\ 2L^2 & \dot{\varepsilon} \gg 1 \end{cases} \quad (37)$$

witnessing a divergence of the elongational viscosity in the Oldroyd-B limit ($L^2 \gg 1$). In figure 2 we present numerical simulations to benchmark these results. The numerical simulations have been carried out in a three dimensional cubic domain with edge H consisting of $H \times H \times H = 20 \times 20 \times 20$ cells. Periodic conditions are applied in all directions. The elongational rate is changed in the range $10^{-6} \leq \dot{\varepsilon} \leq 10^{-2}$ lbu and the polymer relaxation time in the range $10^3 \leq \tau_P \leq 10^5$ lbu, for three values of the finite extensibility parameter, $L^2 = 10, 10^2, 10^4$, and fixed $\eta_P = 0.0$ lbu. Again, the values of the conformation tensor are taken when the simulation has reached a steady state. When reporting the quantity D/Λ_e, i.e. the elongational viscosity scaled by the polymer viscosity, as a function of the dimensionless elongational rate Λ_e, all the numerical simulations collapse
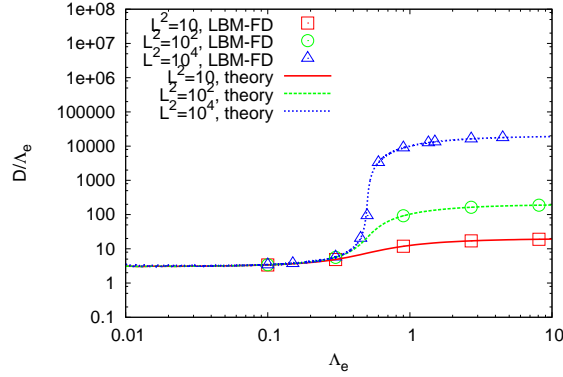
12

FIG. 2: We plot the dimensionless elongational viscosity as a function of the dimensionless elongation rate $\Lambda_e = \tau_P \dot{\varepsilon}$. Symbols are the results of the LBM-FD numerical simulations with different imposed elongational rates, different τ_P and different L^2 (see text for details). All the numerical simulations collapse on different master curves, dependently on the value of L^2: $L^2 = 10$ (squares), $L^2 = 10^2$ (circles) and $L^2 = 10^4$ (triangles). The Lines are the theoretical prediction based on equations (32) and (33).

on different master curves, dependently on the value of L^2. This behaviour is consistent with the theoretical predictions obtained from equations (32) and (33). For small Λ_e the elongational viscosity is just three times the polymer viscosity, while at large Λ_e we approach another constant value dependent on the finite extensibility parameter L^2 (see equation (37)).

C. Small amplitude Oscillatory Shearing

By promoting the shear variable considered in section (III A) to a time-dependent variable, $u_x = \dot{\gamma}(t)y$, $u_y = 0$, $u_z = 0$, we can analyze the behaviour of the polymer field under time-dependent loads. We will then analyze the limit of small amplitudes, i.e. $L \gg 1$. In this limit $Z = 1$ and we are left with the following time-dependent equation

$$
\begin{pmatrix} \sigma_{P,xx} - 1 & \sigma_{P,xy} & 0 \\ \sigma_{P,yx} & \sigma_{P,yy} - 1 & 0 \\ 0 & 0 & \sigma_{P,zz} - 1 \end{pmatrix} + \tau_P \left[\frac{\partial}{\partial t} \begin{pmatrix} \sigma_{P,xx} & \sigma_{P,xy} & 0 \\ \sigma_{P,yx} & \sigma_{P,yy} & 0 \\ 0 & 0 & \sigma_{P,zz} \end{pmatrix} - \dot{\gamma}(t) \begin{pmatrix} 2\sigma_{P,yx} & \sigma_{P,yy} & 0 \\ \sigma_{P,yy} & 0 & 0 \\ 0 & 0 & 0 \end{pmatrix} \right] = 0.
$$

(38)

13

For large t, the equations for the first normal stress difference N and polymer shear stress S defined in section (III A) are therefore

$$\begin{cases} N + \tau_P \partial_t N = 2\tau_P \dot{\gamma}(t) S \\ S + \tau_P \partial_t S = \tau_P \dot{\gamma}(t). \end{cases} \tag{39}$$

Assuming $\dot{\gamma}(t) = \dot{\gamma}^{(0)} \cos(\omega t) = \Re(\dot{\gamma}^{(0)} e^{-i\omega t})$, we find that the stresses needed to maintain the motion will also be oscillatory in nature

$$S = \Re(S^{(0)} e^{-i\omega t}) = \Re(\dot{\gamma}^{(0)} \eta^* e^{-i\omega t}) = \dot{\gamma}^{(0)} \eta' \cos(\omega t) - \dot{\gamma}^{(0)} \eta'' \sin(\omega t)$$

where $\eta^* = \eta' - i\eta''$ is the complex viscosity whose components can be computed by taking S and N as complex variables and considering the real and imaginary part of equation (39)

$$\eta'(\omega) = \frac{\tau_P}{1 + \omega^2 \tau_P^2} \qquad \eta''(\omega) = \frac{\omega \tau_P^2}{1 + \omega^2 \tau_P^2}.$$

The dimensionless storage ($G'(\omega)$) and loss ($G''(\omega)$) moduli [17] are given by

$$G''(\omega) = \omega \eta'(\omega) = \frac{\tau_P \omega}{1 + \omega^2 \tau_P^2} \qquad G'(\omega) = \omega \eta''(\omega) = \frac{(\omega \tau)_P^2}{1 + \omega^2 \tau_P^2}. \tag{40}$$

In figure 3 we present numerical simulations to benchmark these results. The set-up for the numerical simulations is similar to the one presented in section (III A), with three dimensional domains consisting of $2 \times H \times 2$ cells, with variable wall-to-wall gap H. We then apply an oscillatory shear flow $u_x = \dot{\gamma}(t)y = \frac{2U_w}{H} \cos(\omega t)y$, $u_y = u_z = 0$, $\dot{\gamma}(t) = \dot{\gamma}^{(0)} \cos(\omega t)$ at the walls of the LBM simulations and set zero feedback ($\eta_P = 0$ lbu) of the polymers into the fluid. The frequency ω is changed in the range $10^{-6} \leq \omega \leq 10^{-3}$ lbu and the polymer relaxation time in the range $10^3 \leq \tau_P \leq 10^6$ lbu, for a given value of the finite extensibility parameter, $L^2 = 10^5$, fixed $\eta_P = 0.0$ lbu and maximum wall velocity $U_w = 10^{-3}$ lbu. A word of caution is in order, as the assumed flow conditions require that the lattice Boltzmann time to establish a steady shear flow, $\tau_{\nu_S} \sim \frac{H^2}{\nu_S}$ (with ν_S the solvent kinematic viscosity), is much shorter than the period of the oscillations, i.e. $\tau_{\nu_S} \omega \ll 1$, otherwise the shear flow will be found in a transient regime. This condition is achieved by a proper tuning of the solvent kinematic viscosity and the wall gap H in all the numerical simulations. As we can see from figure 3, the dimensionless storage modulus ($G'(\omega)$) and the dimensionless loss modulus ($G''(\omega)$) are in very good agreement with the theoretical prediction of equation (40).
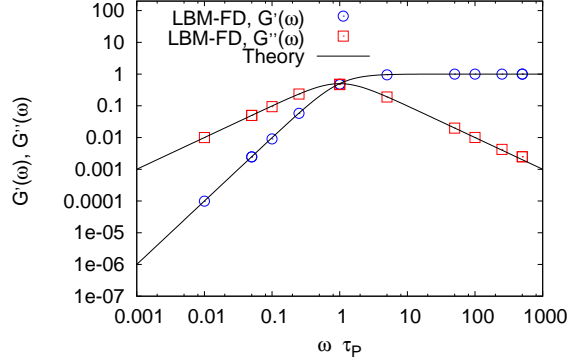
14

FIG. 3: We plot the dimensionless storage modulus ($G'(\omega)$, circles) and the dimensionless loss modulus ($G''(\omega)$, squares) versus the dimensionless frequency $\omega\tau_P$. Results are obtained from the LBM-FD numerical simulations with $L^2 = 10^5$ (Oldroyd-B limit); black lines show the theoretical prediction for the Oldroyd-B model (see equation (40)).

D. Stress relaxation after cessation of steady shear flow

We finally consider a situation with $u_x = \dot{\gamma}(t)y$, $u_y = 0$, $u_z = 0$ with $\dot{\gamma}(t)$ being constant for $t < t_0$, and $\dot{\gamma}(t) = 0$ for $t \geq t_0$. The equations for $t \geq t_0$ are therefore

$$Z\begin{pmatrix} \sigma_{P,xx}-1 & \sigma_{P,xy} & 0 \\ \sigma_{P,yx} & \sigma_{P,yy}-1 & 0 \\ 0 & 0 & \sigma_{P,zz}-1 \end{pmatrix} + \tau_P\frac{\partial}{\partial t}\begin{pmatrix} \sigma_{P,xx} & \sigma_{P,xy} & 0 \\ \sigma_{P,yx} & \sigma_{P,yy} & 0 \\ 0 & 0 & \sigma_{P,zz} \end{pmatrix} - \tau_P\begin{pmatrix} \sigma_{P,xx} & \sigma_{P,xy} & 0 \\ \sigma_{P,yx} & \sigma_{P,yy} & 0 \\ 0 & 0 & \sigma_{P,zz} \end{pmatrix}D_t\log Z = 0.$$

$$(41)$$

We next write down the equations for the variables $S = \sigma_{P,xy}$ and $T = Tr(\boldsymbol{\sigma}_P) - 3$

$$\begin{cases} \frac{L^2+T}{L^2}T + \tau_P\partial_t T - \tau_P(3+T)\frac{\partial_t T}{(L^2+T)} = 0 \\ \frac{L^2+T}{L^2}S + \tau_P\partial_t S - \tau_P S\frac{\partial_t T}{(L^2+T)} = 0. \end{cases} \qquad (42)$$

The first of equations (42) can be solved to get a differential equation for T

$$\frac{\partial_{\tilde{t}}T}{T} = \frac{(L^2+T)^2}{L^2(3-L^2)} \qquad (43)$$

where $\tilde{t} = t/\tau_P$. The Oldroyd-B ($L^2 \gg 1$) limit simply implies an exponential decay $T(t) = T_0 e^{-(t-t_0)/\tau_P}$, where with the subscript 0 we indicate variables at time $\tilde{t} = t_0/\tau_P$. For the general case with finite extensibility parameter L^2 in equation (43), $T(t)$ cannot be written in terms of

15

elementary functions. However, by a proper manipulations of equations (42), is always possible
to get an equation relating the shear stress to the trace of the stress during relaxation [17]

$$\frac{S(t)}{S_0} = \left(\frac{T(t)}{T_0}\right)^{(L^2-3)/L^2} \left(\frac{L^2+T(t)}{L^2+T_0}\right)^{1-(L^2-3)/L^2}.$$ (44)

For completeness, we note that further manipulations [53, 54] of equations (42) allow to show
that the area under the stress-relaxation curve is closely related to the first normal stress-difference
before the cessation of the shear flow

$$N_0(t < t_0) = 2\dot{\gamma} \int_{t_0}^{\infty} S dt = 2\dot{\gamma}\tau_P \int_{t_0/\tau_P}^{\infty} S d\tilde{t}.$$ (45)

In the left panel of figure 4 we plot the time evolution for both $S(t)$ and $T(t)$ versus the dimension-
less time (t/τ_P) in the process of an inception of shear flow with the approaching to the steady state
and subsequent cessation. The set-up for the numerical simulations is similar to the one presented
in section (III A), with three dimensional domains consisting of $L_x \times H \times L_z = 2 \times 60 \times 2$ cells.
The shear is set to $2U_w/H = 10^{-3}$ lbu at time $t/\tau_P = 0$, with the polymer relaxation time $\tau_P = 10^4$
lbu and finite extensibility parameter $L^2 = 4.1$. The value of L^2 is chosen to create a net distinction
between the time evolution of $S(t)$ and $T(t)$, that otherwise would be identical in the Oldroyd-B
limit ($L^2 \gg 1$, see also equation (44)). The feedback of the polymer into the fluid is set to zero. For
$t/\tau_P = 10$ (that means $t_0 = 10\tau_P$ in the above equations) the system is surely under the effect of a
steady shear flow. At that time, the shear is suddenly switched off and the system starts decaying.
The decay process is illustrated in the right panel of figure 4, where we compare the results of the
numerical simulations with the analytical predictions obtained from equations (43) and (44).

IV. BINARY MIXTURES WITH VISCOELASTIC PHASES

In this section we describe problems where both phase segregation and viscoelasticity are
present. First of all we switch on phase segregation: when $\mathcal{G} > \mathcal{G}_c$ in equation (6), with $\mathcal{G}_c$ a
critical value of the coupling constant, the resulting physical domain is partitioned into two differ-
ent subdomains, each with a majority of one of the two components, with the interface between
the two components described as a thin layer of thickness ξ where the fluid properties change
smoothly. The values of the interface thickness and the mobility μ (see equation (4)) need to be
larger than those suggested by physical considerations in order to make the simulations affordable.
They are empirically tuned in order to match the analytical predictions of sharp-interface hydro-
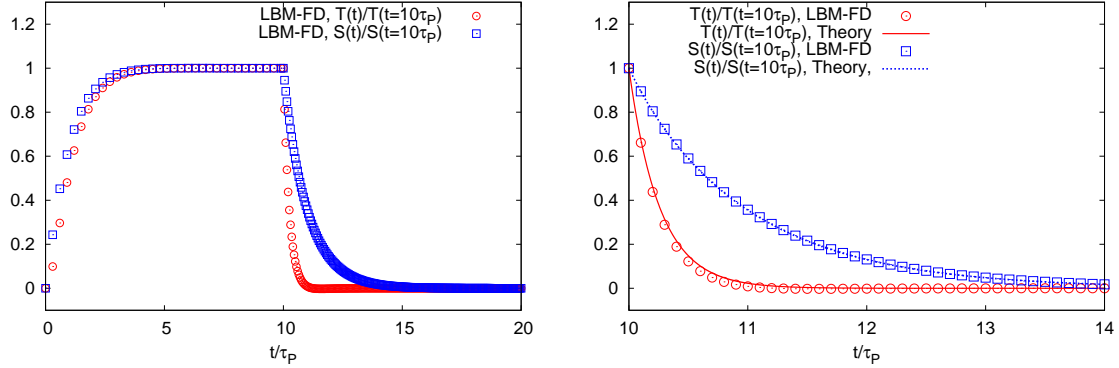dynamics (see later).

16

FIG. 4: We plot the time evolution for the polymer shear stress $S(t)$ (squares) and the excess trace $T(t) = Tr(\boldsymbol{\sigma}_P) - 3$ (circles) versus the dimensionless time (t/τ_P) during the inception of a shear flow and subsequent cessation (see text for details). The shear starts at time $t = 0$ and for $t/\tau_P = 10$ the system is under the effect of a steady shear flow. At time $t/\tau_P = 10$ the shear is suddenly switched off and the system starts decaying. The decay process is better illustrated in the right panel where we compare the results of the numerical simulations with the analytical predictions obtained from equations (43) and (44).

We will then apply our numerical approach to the characterization of deformation of droplets in confined geometries, where the involved phases may possess a viscoelastic nature. This is a relevant problem, for example, when determining the properties of emulsions microstructures [56, 57]. Emulsions play an important role in a huge variety of applications, including foods, cosmetics, chemical and material processing [15]. Deformation, break-up and coalescence of droplets occur during flow, and the control over these processes is imperative to synthesize the desired macroscopic behaviour of the emulsion. Most of the times, the synthesis of the emulsion takes place in presence of confinement, and relevant constituents have commonly a viscoelastic -rather than Newtonian- nature. The "single" drop problem has been considered to be the simplest model: in the case of dilute emulsions with negligible droplets interactions, the dynamics of a single drop indeed provides complete information about the emulsion behaviour. Single drop deformation has been extensively studied and reviewed in the literature for the case of Newtonian [58–61] and also non-Newtonian fluids [42, 43, 46, 62].

17

A. Effects of confinement on droplet deformation

In the classical problem studied by Taylor [58], a droplet with radius R, interfacial tension σ, and viscosity η_D is suspended in another immiscible fluid matrix with viscosity η_M under the effect of a shear flow with intensity $\dot{\gamma}$ (see left panel of figure 5). The various physical quantities are grouped in two dimensionless numbers, the Capillary number

$$Ca = \frac{\dot{\gamma} R \eta_M}{\sigma} \tag{46}$$

giving a dimensionless measure of the balance between viscous and interfacial forces, and the viscous ratio $\lambda = \eta_D / \eta_M$, going from zero for vanishing values of the droplet viscosity (i.e. a bubble) to infinity in the case of a solid particle. In order to quantify the deformation of the droplet, we study the deformation parameter $D = (a - b)/(a + b)$, where a and b are the droplet semi-axes in the shear plane, and the orientation angle θ between the major semi-axis and the flow direction (see also the left panel of figure 5). Taylor's result, based on a small deformation perturbation analysis to first-order, relates the deformation parameter to the Capillary number Ca,

$$D = \frac{(19\lambda + 16)}{(16\lambda + 16)} Ca \tag{47}$$

whereas the orientation angle is constant and equal to $\theta = \pi/4$ to first order. Taylor's analysis was later extended by working out the perturbation analysis to second order in Ca, which leaves unchanged the expression of the deformation parameter (47) and gives the $\mathcal{O}(Ca)$ correction to the orientation angle [63, 64]. The effects of confinement have been theoretically addressed at $\mathcal{O}(Ca)$ by Shapira and Haber [44, 65]. They found that the deformation parameter in a confined geometry can be obtained by the Taylor's result through a correction in the power of the ratio between the droplet radius at rest R and gap between the walls H

$$D = \frac{(19\lambda + 16)}{(16\lambda + 16)} \left[1 + C_{sh} \frac{2.5\lambda + 1}{\lambda + 1} \left(\frac{R}{H} \right)^3 \right] Ca \tag{48}$$

where C_{sh} is a tabulated numerical factor depending on the relative distance between the droplet center and the wall (the value of C_{sh} for droplets placed halfway between the plates is $C_{sh} = 5.6996$).

LBM have already been used to model the droplet deformation problems [66–69]. Three-dimensional numerical simulations of the classical Taylor's problem [58] have been performed by Xi & Duncan [66] using the "Shan-Chen" approach [7, 8]. The single droplet problem was also

18

investigated by Van Der Sman & Van Der Graaf [67] using a "free energy" LBM. LBM modelling of two phase flows is intrinsically a diffuse interface method and involves a finite thickness of the interface between the two liquids and related free-energy model parameters. These model parameters are characterized by two dimensionless numbers: the Péclet (Pe) and Cahn numbers (Ch), the Cahn number is the interface thickness normalized with the droplet radius, whereas the Péclet number Pe is the ratio between the convective time scale and the interface diffusion. A recent comprehensive study by Komrakova *et al.* has investigated the influence of Pe, Ch and mesh resolution on the accuracy and stability of the numerical simulations. Drops of moderate resolution (radius less than 30 lattice units) require smaller interface thickness, while a thicker interface should be used for highly resolved drops. Those parameters have to be within certain ranges to reproduce the physical behavior [67, 68] of sharp-interface hydrodynamics [70]. Since our aim is to quantify and explore the importance of viscoelasticity in our simulations, we choose the aforementioned parameters in such a way that the Newtonian (sharp-interface) predictions for droplet orientation and deformation are well reproduced.

All the simulations described in the following sections refer to cases with polymer relaxation times ranging in the interval $0 \leq \tau_P \leq 4000$ lbu and finite extensibility $10 \leq L^2 \leq 10^4$. The numerical simulations have been carried out in three dimensional domains with $L_x \times H \times H = 288 \times 128 \times 128$ lattice cells. The droplet radius R has been changed in the range $30 \leq R \leq 40$ lattice cells with fixed H to achieve different confinement ratios $2R/H$. Periodic conditions are applied in the stream-flow (x) and in the transverse-flow (z) directions. The droplet is subjected to a linear shear flow $u_x = \dot{\gamma}y$, $u_y = u_z = 0$, with the shear introduced with two opposite velocities in the stream-flow direction ($u_x(x, y = 0, z) = -u_x(x, y = H, z) = U_w$) at the upper ($y = H$) and lower wall ($y = 0$). For the numerical simulations presented we have used $\mathscr{G} = 1.5$ lbu in (6)(the critical point is at $\mathscr{G}_c = 1.0$ for the parameters chosen), corresponding to a surface tension $\sigma = 0.09$ lbu and associated bulk densities $\rho_A = 2.0$ lbu and $\rho_B = 0.1$ lbu in the A-rich region.

In the right panel of figure 5 we report the steady state deformation parameter D for a Newtonian droplet under steady shear as a function of the associated Capillary number Ca for two different confinement ratios: $2R/H = 0.46$ and $2R/H = 0.7$. The viscous ratio between the droplet phase and the matrix phase is fixed to $\lambda = \eta_D/\eta_M = \eta_A/\eta_B = 1$, with the dynamic viscosities equal to $\eta_A = \eta_B = 1.74$ lbu. The linearity of the deformation is captured by the numerical simulations up to the largest Ca considered, but the numerical results overestimate Taylor's prediction (referred to as "Newtonian Unconfined"), being well approximated by the theoretical prediction of Shapira

& Haber for a confined droplet [44] (refereed to as "Newtonian confined"). For completeness, we also report a comparison with the steady state deformation prediction of a model proposed recently by Minale [45], describing the dynamics (and steady states) of a droplet under the assumption that it deforms into an ellipsoid. This model belongs to the family of "ellipsoidal" models [71], which were originally introduced to describe the dynamics of a single Newtonian drop immersed in a matrix subjected to a generic flow field. The steady state predictions of such models for small Ca are constructed in such a way to recover the exact perturbative result, i.e. Taylor's result for an unbounded droplet [72] or the Shapira & Haber result for a confined droplet [45]. The prediction of these ellipsoidal models is hardly distinguishable from the perturbative results [44] in these Newtonian cases, at least for the range of parameters that we have used in the numerical simulations. Nevertheless, these models will be quite useful when discussing the influence of viscoelasticity on droplet deformation and orientation, as will be done in the following sections.

B. Effects of Viscoelasticity on droplet deformation and orientation

In this section we look at the effects of viscoelasticity in droplet deformation. We will separately address the importance of matrix viscoelasticity and droplet viscoelasticity, using the proposed methodology described in section II, and compare with some of the theoretical predictions available in the literature [42, 43, 46]. Again, we work with unitary viscous ratio, defined in terms of the total (fluid+polymer) shear viscosity: $\lambda = (\eta_A + \eta_P)/\eta_B = 1$, in case of droplet viscoelasticity; $\lambda = \eta_A/(\eta_B + \eta_P) = 1$, in case of matrix viscoelasticity. Viscoelastic effects show up in the droplet deformation and orientation in terms of two dimensionless parameters: the Deborah number,

$$De = \frac{N_1 R}{2\sigma} \frac{1}{Ca^2} \tag{49}$$

where N_1 is the first normal stress difference generated in simple shear slow [17], and the ratio N_2/N_1 between the second and first normal stress difference [42]. Solving the constitutive equation for steady shear (see section (III A)), the first normal stress difference for the FENE-P model [17, 55] can be computed (see subsection (III A) and equation (28)), while $N_2/N_1 = 0$. In the Oldroyd-B limit ($L^2 \gg 1$) we can use the asymptotic expansion of the hyperbolic functions and we get $N_1 = 2\eta_P \dot{\gamma}^2 \tau_P$ so that

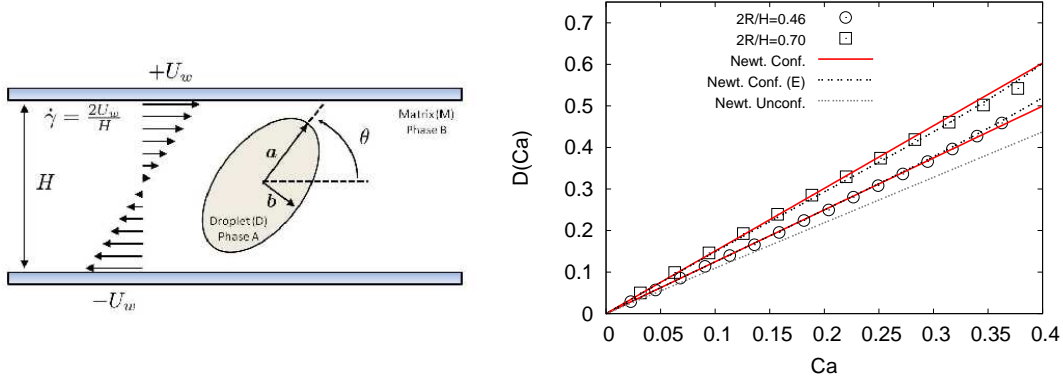$$De = \frac{\tau_P}{\tau_{em}} \frac{\eta_P}{\eta_M} \tag{50}$$

20

FIG. 5: Left Panel: shear plane $(z = H/2)$ view of the numerical set-up for the study of deformation of confined droplets. A Newtonian droplet (Phase A) with radius R and shear viscosity η_A is placed in between two parallel plates at distance H in a Newtonian matrix (Phase B) with shear viscosity η_B. We then add a polymer phase with shear viscosity η_P in the droplet or matrix phase. We work with unitary viscous ratio, defined in terms of the total (fluid+polymer) shear viscosity: $\lambda = (\eta_A + \eta_P)/\eta_B = 1$, in case of droplet viscoelasticity; $\lambda = \eta_A/(\eta_B + \eta_P) = 1$, in case of matrix viscoelasticity. A shear is applied by moving the two plates in opposite directions with velocities $\pm U_w$. Right panel: We report the steady state deformation parameter D for a Newtonian droplet in a Newtonian matrix ($\eta_P = 0.0$ lbu) under steady shear as a function of the associated Capillary number Ca. For small Ca the linearity of the deformation is captured by the numerical simulations, but the numerical results overestimate Taylor's prediction (referred to as "Newtonian Unconfined"), being well approximated by the theoretical prediction of Shapira & Haber for a confined droplet [44] (referred to as "Newtonian confined"). Two confinement ratios are considered: $2R/H = 0.46$ and $2R/H = 0.7$. We also report the theoretical predictions of the "ellipsoidal" models [45, 71] (referred to as "Newtonian confined (E)"). For the "confined" theoretical prediction, larger deformations are related to larger confinement ratio.

showing that De is clearly dependent on the ratio between the polymer relaxation time τ_P and the emulsion time $\tau_{em} = \frac{R\eta_M}{\sigma}$, the latter depending on the interface properties (i.e. surface tension). For finite L^2, however, we need to use the definition of De based on the first normal stress difference (see section (III A)). Benchmark tests for the viscoelastic effects will be proposed for both shear-induced droplet deformation and orientation at small Ca, although the effects on droplet orientation will be more pronounced. This is because non-Newtonian effects on the drop steady state deformation show up at the second order in Ca, while the orientation angle has a correction

21

at first order in Ca [42, 62]. In particular, to test both confinement and viscoelastic effects, we will also refer to the model proposed by Minale, Caserta & Guido [46] for ellipsoidal droplets. Indeed, the aforementioned ellipsoidal models for Newtonian fluids have been recently proposed also for non-Newtonian fluids. In particular, Minale [43] proposed an ellipsoidal model which recovers, in the small Ca-limit, the steady state theory developed by Greco [42]. Minale, Caserta & Guido [46] proposed a phenomenological model to study the effects of confinement in non-Newtonian systems, which generalizes the work by Minale [43] originally developed for Newtonian systems. We start with the effect of droplet viscoelasticity. For a given confinement ratio, $2R/H = 0.46$, in figure 6 we report the steady state droplet deformation and orientation angle. We use the Oldroyd-B model, by choosing a large value of $L^2 = 10^4$, and consider two relaxation times in the polymer equation (3), $\tau_P = 2000$ lbu and $\tau_P = 4000$ lbu, corresponding to Deborah numbers (based on equation (50)) $De = 1.42$ and $De = 2.84$, respectively. The polymer viscosity is kept fixed to $\eta_P = 0.6933$ lbu, corresponding to a polymer concentration of $\eta_P/(\eta_A + \eta_P) = 0.4$. The deformation computed from the numerical simulations reveals a small effect of viscoelasticity, which is consistent with the theoretical prediction of the model by Minale, Caserta & Guido [46] (referred to as "non-Newtonian confined (E)"). In particular, with respect to the Newtonian case, deformation is slightly inhibited by viscoelasticity and overestimates Greco's prediction for an unconfined non-Newtonian droplet [42] (referred to as "non-Newtonian unconfined"). As for the orientation, we hardly see any effect, which is in line with the prediction of the theoretical models reported for the two different Deborah numbers. These observations echo other experimental and numerical results present in the literature on the effect of droplet viscoelasticity on deformation and orientation [73–76].

We next look at the effect of matrix viscoelasticity, figures 7 and 8. In figure 7 we report the steady state droplet deformation for two different confinement ratios: $2R/H = 0.46$ (left panel) and $2R/H = 0.7$ (right panel). Again, we choose a large value of $L^2 = 10^4$, and consider a relaxation time $\tau_P = 2000$ lbu in the polymer equation (3), corresponding to different Deborah numbers, depending on the droplet radius (see equation (50)): $De = 1.42$ for $2R/H = 0.46$ and $De = 1.42$ for $2R/H = 0.7$. The polymer viscosity is kept fixed to $\eta_P = 0.6933$ lbu, corresponding to a polymer concentration of $\eta_P/(\eta_P + \eta_B) = 0.4$. In both cases, matrix viscoelasticity inhibits droplet deformation with respect to the corresponding Newtonian cases. Also, the unconfined theory by Greco [42] underestimates the deformation, and the mismatch is larger with the larger confinement ratio, as one would have expected since the theory of Greco does not take into account confinement. The
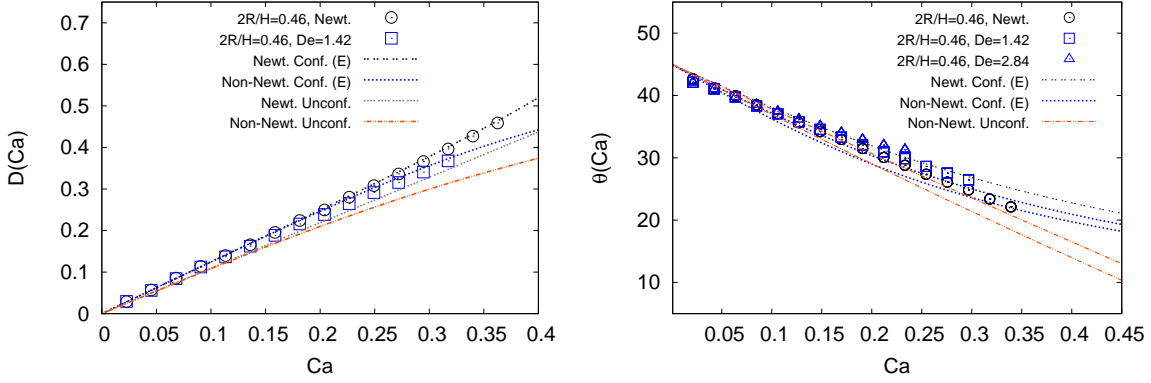
22

FIG. 6: We report the steady state deformation parameter D (left panel, see text for details) and the orientation angle (right panel) for a viscoelastic droplet in a Newtonian matrix under steady shear as a function of the associated Capillary number Ca. The viscous ratio between the droplet phase and the matrix phase is kept fixed to $\lambda = \eta_D / \eta_M = 1$, the confinement ratio is $2R/H = 0.46$. We consider two relaxation times in the polymer equation (3), $\tau_P = 2000$ lbu and $\tau_P = 4000$ lbu, corresponding to Deborah numbers (based on equation (50)) $De = 1.04$ and $De = 2.08$ respectively. The polymer viscosity is kept fixed to $\eta_P = 0.6933$ lbu, corresponding to a polymer concentration of $\eta_P / (\eta_P + \eta_B) = 0.4$. With respect to the Newtonian case, deformation is inhibited by viscoelasticity and the numerical results overestimate Greco's prediction for an unconfined non-Newtonian droplet [42] (referred to as "non-Newtonian unconfined"). As for the orientation, we hardly see any effect. We also report the theoretical predictions of the "ellipsoidal" models [45, 46] for both Newtonian [45] and non-Newtonian [46] cases (referred to as "Newtonian confined (E)" and "non-Newtonian confined (E)"). For the non-Newtonian theoretical prediction, smaller angles are related to larger Deborah number.

model by Minale, Caserta & Guido [46] follows the numerical data with a mismatch emerging at large Ca for the larger confinement ratio: most probably this is due to the fact that confinement starts to act in promoting deformation with shapes departing from an ellipsoid [65]. A non trivial interplay between confinement and viscoelasticity is also visible from figure 9, where we report the steady state snapshots for the polymer feedback stress of equation (2) for the cases studied in figures 7 and 8. In figure 8 we report the orientation angle for the same cases studied in figure 7. The effect of viscoelasticity is now much more visible, if compared with the case of droplet viscoelasticity reported in figure 6. We also analyze the effect of increasing the relaxation time τ_P in equation (3) for both the confinement ratios studied, which translates in a larger Deborah
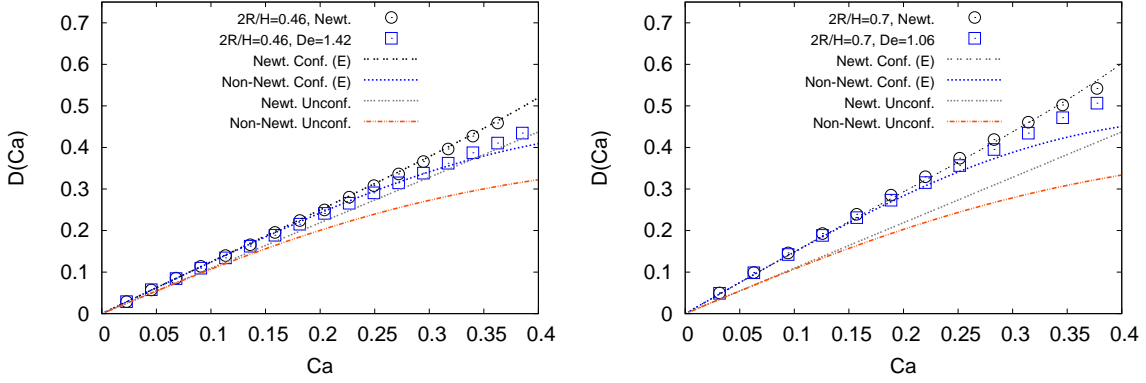
23

FIG. 7: We report the steady state deformation parameter D (see text for details) for a Newtonian droplet in a Viscoelastic matrix under steady shear as a function of the Capillary number Ca. The viscous ratio between the droplet phase and the matrix phase is kept fixed to $\lambda = \eta_D/\eta_M = 1$. Two different confinement ratios are considered: $2R/H = 0.46$ (left panel) and $2R/H = 0.7$ (right panel). Again, as already done for the data of figure 6, we choose a large value of the finite extensibility parameter $L^2 = 10^4$, and consider a relaxation time in the polymer equation (3) $\tau_P = 2000$ lbu. The corresponding Deborah numbers depend on the droplet radius, based on equation (50): $De = 1.42$ for $2R/H = 0.46$ and $De = 1.42$ for $2R/H = 0.7$. The polymer viscosity is kept fixed to $\eta_P = 0.6933$ lbu, corresponding to a polymer concentration of $\eta_P/(\eta_P + \eta_B) = 0.4$. The numerical results overestimate Greco's prediction for an unconfined non-Newtonian droplet [42] (referred to as "non-Newtonian unconfined"). We also report the prediction of "ellipsoidal" models [45, 46] for both Newtonian [45] and non-Newtonian [46] cases (referred to as "Newtonian confined (E)" and "non-Newtonian confined (E)").

number. The change in the orientation angle for the Newtonian cases is linear in Ca up to the largest Ca considered, which is consistent with the linearity of the deformation discussed in figure 5. This generates a mismatch with the corresponding Ellipsoidal model predictions [45]: just to give some quantitative numbers, for a Capillary number $Ca = 0.35$, there is a mismatch of $2 - 3°$ in the smaller confinement ratio, which becomes roughly doubled (i.e. $5 - 6°$) for the larger confinement ratio. The orientation angle in the non-Newtonian cases, instead, is better captured by the ellipsoidal model by Minale, Caserta & Guido [46]. Overall, in both the Newtonian and non-Newtonian cases, the mismatch between the numerical results and the prediction of the ellipsoidal models is more pronounced at large confinement ratios (right panel of figure 8), an observation that echoes the discussion done for the data of figure 7.
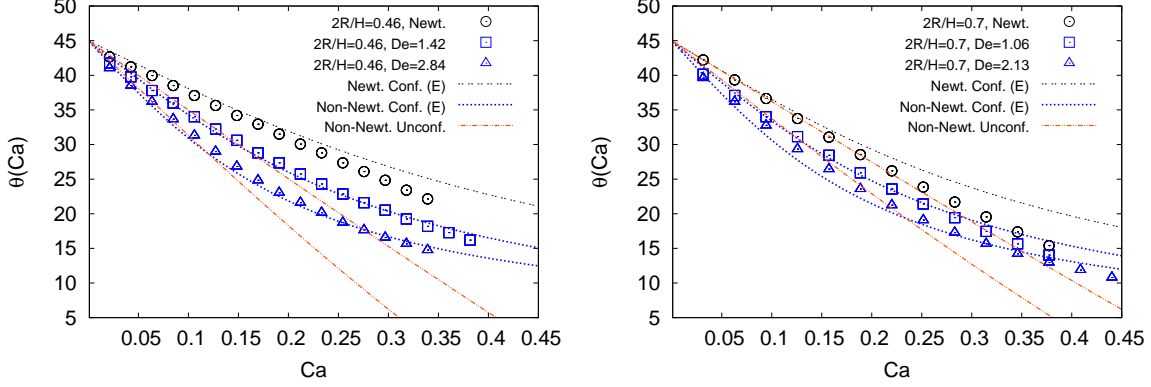
24

FIG. 8: We report the steady state orientation angle for a Newtonian droplet in a Viscoelastic matrix under steady shear as a function of the Capillary number Ca. The viscous ratio between the droplet phase and the matrix phase is kept fixed to $\lambda = \eta_D/\eta_M = 1$. Two different confinement ratios are considered: $2R/H = 0.46$ (left panel) and $2R/H = 0.7$ (right panel). Data are the same as those of figure 7, plus some other data obtained by increasing the relaxation time τ_P in equation (3). For a given Ca, the numerical results overestimate Greco's prediction for an unconfined non-Newtonian droplets [42] (referred to as "non-Newtonian unconfined"). We also report the theoretical predictions of the "ellipsoidal" models [45, 46] for both Newtonian and non-Newtonian cases (referred to as "Newtonian confined (E)" and "non-Newtonian confined (E)"). For the non-Newtonian theoretical prediction, smaller angles are related to larger Deborah number.

Finally, we want to address and test the importance of the finite extensibility parameter in the polymer equation (3). For a given confinement ratio $2R/H = 0.46$ and $\tau_P = 2000$ lbu in equation (3), we have repeated the numerical simulations described in the left panel of figure 7 for a finite extensibility parameter $L^2 = 10$. As L decreases, the polymer dumbell becomes less extensibile and the maximum level of stress attainable is reduced. There are some consequences. First, we cannot rely on equation (50) to define the Deborah number, which strictly holds only in the large-L^2 limit. Second, at large shears, the model exhibits thinning effects, as predicted and verified in subsection (III A), and the definition of the Capillary number (46) given in terms of the matrix viscosity has to be changed to include such effects. Indeed, by using the definition of the Deborah number given in equation (50) and a shear independent matrix viscosity in equation (46) in the theoretical models, the agreement between the numerical results and the theory deteriorates (see left panel of figure 10, whereas the large-L^2 case was well in agreement. In the right panel of figure

25

Feedback Stress Magnitude

(a) 2R/H=0.46, Ca= 0.17 , De=0.71

(b) 2R/H=0.7, Ca= 0.23 , De=0.53

(c) 2R/H=0.46, Ca= 0.17 , De=1.42

(d) 2R/H=0.7, Ca= 0.23 , De=1.06

(e) 2R/H=0.46, Ca= 0.17 , De=2.84
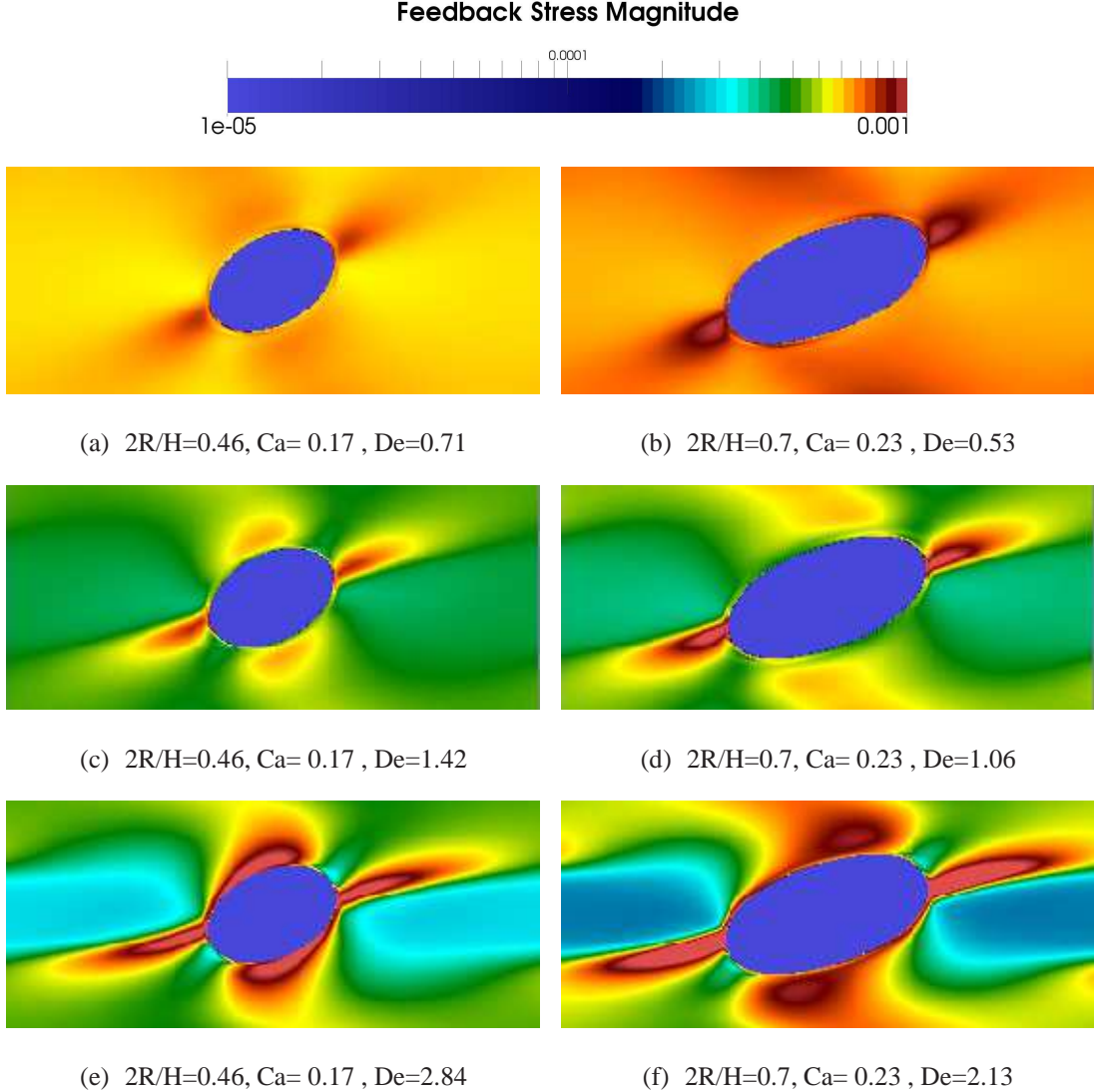
(f) 2R/H=0.7, Ca= 0.23 , De=2.13

FIG. 9: We report the steady state snapshots of the polymer feedback stress in equation (2) for the cases studied in figures 7 and 8 in the plane $z = H/2$. Results are obtained for the same wall velocity, $U_w = \pm 0.02$ lbu, the same finite extensibility parameter $L^2 = 10^4$, and considering three different relaxation times in the polymer equation (3), $\tau_P = 1000, 2000, 4000$ lbu. The corresponding Deborah numbers depend on the droplet radius, based on equation (50): $De = 0.71, 1.42, 2.84$ for $2R/H = 0.46$ and $De = 0.53, 1.06, 2.13$ for $2R/H = 0.7$.

.

10 we report the same data, by changing: (i) the definition of Capillary in equation (46), based on the thinning effects analyzed in subsection (III A); (ii) the definition of the Deborah number, which is now computed according to equation (49), with the first normal stress difference given
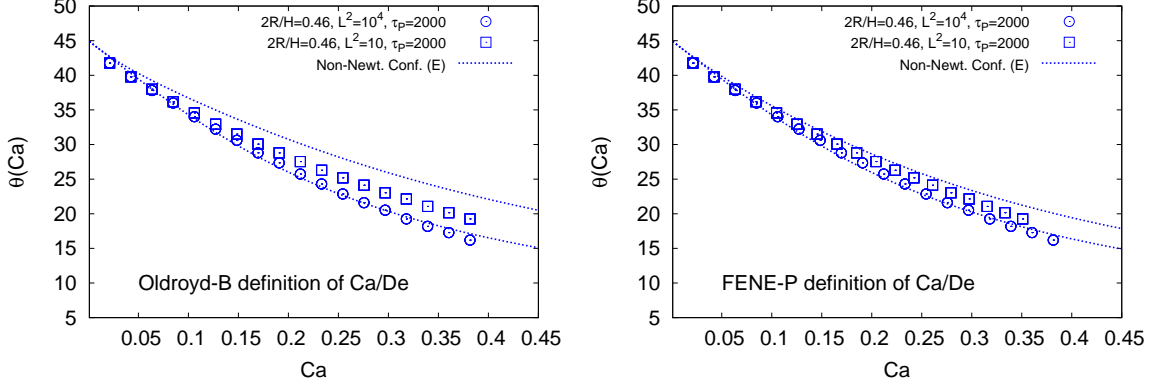
FIG. 10: Left Panel: we report the steady state orientation angle for a Newtonian droplet in a Viscoelastic matrix under steady shear as a function of the Capillary number Ca. For a given confinement ratio $2R/H = 0.46$ and $\tau_P = 2000$ lbu in equation (3), we have repeated the numerical simulations described in the left panel of figure 7 for a finite extensibility parameter $L^2 = 10$. We have used the definition of Deborah number based on equation (50) and a shear independent matrix viscosity in equation (46) to compute Ca. These choices are appropriate only in the Oldroyd-B limit ($L^2 \gg 1$), hence referred to as "Oldroyd-B definition". Right Panel: we report the same data of the left panel by changing the definition of Capillary number in equation (46), based on the thinning effects analyzed in section (III), and changing the definition of the Deborah number which is now computed according to equation (49). This is referred to as "FENE-P definition". Steady state snapshots of the polymer feedback stress in equation (2) for some of these cases are reported in figure 11.

in (28). As one can see the agreement gets better, especially at small Ca. For completeness, in figure 11, we report the steady state snapshots for the polymer feedback stress of equation (2) for the cases studied in figure 10.

V. CONCLUSIONS

We have proposed numerical simulations of viscoelastic fluids based on a hybrid algorithm combining lattice-Boltzmann models (LBM) and Finite Differences (FD) schemes, the former used to model the macroscopic hydrodynamic equations, and the latter used to model the kinetics of polymers using the constitutive equations for finitely extensible non-linear elastic dumbells with Peterlin's closure (FENE-P). We have first benchmarked the numerical scheme with the char-

Feedback Stress Magnitude

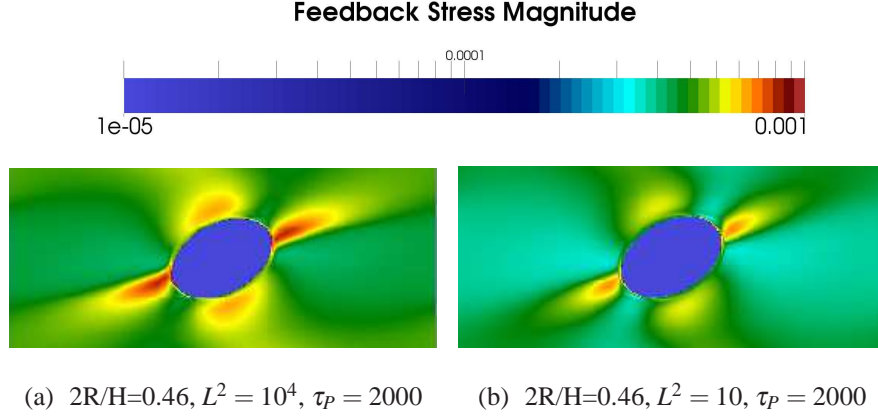(a) 2R/H=0.46, $L^2 = 10^4$, $\tau_P = 2000$ (b) 2R/H=0.46, $L^2 = 10$, $\tau_P = 2000$

FIG. 11: We report the steady state snapshots of the polymer feedback stress in equation (2) for the cases studied in figure 10 in the plane $z = H/2$. Results are obtained for the same wall velocity, $U_w = \pm 0.02$ lbu, the same relaxation time $\tau_P = 2000$ lbu in the polymer equation (3), and different finite extensibility parameters $L^2 = 10$ and $L^2 = 10^4$. The corresponding Deborah numbers depend on the droplet radius, based on equation (49). In both cases, the polymer viscosity is kept fixed to $\eta_P = 0.6933$ lbu, corresponding to a polymer concentration of $\eta_P/(\eta_P + \eta_B) = 0.4$, but the case with $L^2 = 10$ has thinning effects in regions with large shears (see also section (III)).

.

acterization of the rheological properties of a dilute homogeneous solution under steady shear, steady elongational flows, oscillatory flows and transient shear. We then continued to study the model in presence of non-ideal multicomponent interfaces, where immiscibility is introduced in the LBM description using the "Shan-Chen" model [7, 8, 40]. We have characterized the effect of viscoelasticity in droplet deformation under steady shear, by comparing the results of numerical simulations with available theoretical models in the literature [42–47, 58]. Overall, the numerical simulations well capture both the effects of confinement and viscoelasticity, thus exploring problems where the capabilities of LBM were never quantified before. As an upgrade of complexity, it would be extremely interesting to study time-dependent situations [74, 77, 78], other flows in confined geometries [79, 80] and problems where droplet break-up is involved [78]. Complementing these kind of experimental results with the help of numerical simulations would be of extreme interest. Simulations provide easy access to quantities such as drop deformation and orientation as well as the velocity flow field, pressure field, and polymers feedback stresses, inside and outside the droplet. They can be therefore useful to perform in-silico comparative studies, at changing the model parameters, to shed lights on the complex properties of viscoelastic flows in confined

28

geometries.

VI. ACKNOWLEDGEMENTS

References

[1] R. Benzi, S. Succi, and M. Vergassola, Physics Reports **222**, 145 (1992).

[2] S. Succi, *The Lattice Boltzmann Equation for Fluid Dynamics and Beyond* (Oxford University Press, 2001).

[3] D. Wolf-Gladrow, *Lattice-Gas Cellular Automata and Lattice Boltzmann Models: An Introduction* (Springer Verlag, 2001).

[4] S. Chen and G. D. Doolen, Annu. Rev. Fluid Mech. **30**, 329 (1998).

[5] C. K. Aidun and J. R. Clausen, Annu. Rev. Fluid Mech. **42**, 439 (2010).

[6] J. Zhang, Microfluid Nanofluid **10**, 1 (2011).

[7] X. Shan and H. Chen, Phys. Rev. E **47**, 1815 (1993).

[8] X. Shan and H. Chen, Phys. Rev. E **49**, 2941 (1994).

[9] L. Biferale, P. Perlekar, M. Sbragaglia, and F. Toschi, Phys. Rev. Lett. **108**, 104502 (2012).

[10] M. Sbragaglia, R. Benzi, M. Bernaschi, and S. Succi, Soft Matter **8**, 10773 (2012).

[11] M. Sega, M. S. S. S. Kantorovich, and A. O. Ivanovd, Soft Matter **9**, 10092 (2013).

[12] M. Gross, M. E. Cates, F. Varnik, and R. Adhikari, Journal of Statistical Mechanics: Theory and Experiment p. P03030 (2011).

[13] B. Dünweg, U. D. Schiller, and A. J. Ladd, Computer Physics Communications **180**, 605 (2008).

[14] G. Kaehler and A. J. Wagner, Phys. Rev. E **87**, 063310 (2013).

[15] R. G. Larson, *The Structure and Rheology of Complex Fluids* (Oxford University Press, 1999).

[16] A. Peterlin, Polymer **2**, 257 (1961).

[17] R. B. Bird, R. C. Armstrong, and O. Hassager, *Dynamics of polymeric liquids* (J. Wiley & Sons, 1987).

[18] J. G. Oldroyd, Proc. R. Soc. London, Ser. A **200**, 523 (1950).

[19] T. Vaithianathan and L. R. Collins, Journal Computational Physics **187**, 1 (2003).

[20] M. Tomé, L. Grossi, A. Castelo, J. Cuminato, S. McKee, and K. Walters, J. Non-Newtonian Fluid Mech. **141**, 148 (2007).

[21] P. J. Oliveira, J. Non-Newtonian Fluid Mech. **101**, 113 (2001).

[22] P. Yue, J. J. Feng, C. Liu, and J. Shen, J. Fluid Mech. **515**, 293 (2004).

[23] P. Yue, J. J. Feng, C. Liu, and J. Shen, J. Fluid Mech. **540**, 427 (2005).

[24] B. Purnode and M. J. Crochet, J. Non-Newtonian Fluid Mech. **77**, 1 (1998).

[25] C. Chauviére and R. G. Owens, J. Non-Newtonian Fluid Mech. **95**, 1 (2000).

[26] Y. H. Qian and Y.-F. Deng, Phys. Rev. Lett. **79**, 2742 (1997).

[27] I. Ispolatov and M. Grant, Phys. Rev. E **65**, 056704 (2002).

[28] L. Giraud, D. d'Humiéres, and P. Lallemand, Int. J. Mod. Phys. C **8**, 805 (1997).

[29] L. Giraud, D. d'Humiéres, and P. Lallemand, Europhys. Lett. **42**, 625 (1998).

[30] P. Lallemand, D. d'Humiéres, L.-S. Luo, and R. Rubinstein, Phys. Rev. E **67**, 021203 (2003).

[31] O. Malaspinas, N. Fiétier, and M. Deville, J. Non-Newtonian Fluid Mech. **165**, 1637 (2010).

[32] C. Denniston, E. Orlandini, and J. M. Yeomans, Phys. Rev. E **63**, 056702 (2001).

[33] D. Marenduzzo, E. Orlandini, M. E. Cates, and J. M. Yeomans, Phys. Rev. E **76**, 031921 (2007).

[34] J. Onishi, Y. Chen, and H. Ohashi, Prog. Comp. Fluid Dyn. **5**, 75 (2005).

[35] J. Onishi, Y. Chen, and H. Ohashi, Physica A **362**, 84 (2006).

[36] S. Singh, G. Subramanian, and S. Ansumali, Phys. Rev. E **88**, 013301 (2013).

[37] T. T. Pham, U. D. Schiller, J. R. Prakash, and B. Dünweg, Journal of Chemical Physics **131**, 164114 (2009).

[38] A. E. Gunstensen, D. H. Rothman, and S. Zaleski, Phys. Rev. A **43**, 4320 (1991).

[39] H. Liu, A. J. Valocchi, and Q. Kang, Phys. Rev. E **85**, 046309 (2012).

[40] R. Benzi, M. Sbragaglia, S. Succi, M. Bernaschi, and S. Chibbaro, Jour. Chem. Phys. **131**, 104903 (2009).

[41] M. R. Swift, E. Orlandini, W. R. Osborn, and J. M. Yeomans, Phys. Rev. E **54**, 5041 (1996).

[42] F. Greco, J. Non-Newtonian Fluid Mech. **107**, 111 (2002).

[43] M. Minale, J. Non-Newtonian Fluid Mech. **123**, 151 (2004).

[44] M. Shapira and S. Haber, Int J Multiph Flow **16**, 305 (1990).

[45] M. Minale, Rheol. Acta **47**, 667 (2008).

[46] M. Minale, S. Caserta, and S. Guido, Langmuir **26**, 126 (2010).

[47] M. Minale, Rheol Acta **49**, 789 (2010).

[48] M. Sbragaglia and D. Belardinelli, Phys. Rev. E **88**, 013306 (2013).

[49] K. Premnath and J. Abraham, Journal of Computational Physics **224**, 539 (2007).

[50] M. L. Porter, E. T. Coon, Q. Kang, J. D. Moulton, and J. W. Carey, Phys. Rev. E **86**, 036701 (2012).

[51] B. Dünweg, U. D. Schiller, and A. J. C. Ladd, Phys. Rev. E **76**, 036704 (2007).

[52] P. Perlekar, D. Mitra, and R. Pandit, Phys. Rev. Lett. **97**, 264501 (2006).

[53] R. Bird, P. Dotson, and R. Armstrong, Journal of Non-Newtonian Fluid Mechanics **7**, 213 (1980).

[54] M. Herrchen and H. Oettinger, J. Non-Newtonian Fluid Mech. **68**, 17 (1997).

[55] A. Lindner, J. Vermant, and D. Bonn, Physica A **319**, 125 (2003).

[56] G. F. Christopher and S. L. Anna, J Phys D Appl Phys **40**, R319 (2007).

[57] R. Seemann, M. Brinkmann, T. Pfohl, and S. Herminghaus, Rep. Prog. Phys. **75**, 016601 (2012).

[58] G. I. Taylor, Proc. Royal Soc A **138** (1932).

[59] H. P. Grace, Chem. Eng. Commun. **14**, 225 (1982).

[60] H. A. Stone, Annu. Rev. Fluid Mech. **26**, 65 (1994).

[61] J. M. Rallison, Annu. Rev. Fluid Mech. **16**, 45 (1984).

[62] S. Guido, Current Opinion in Colloid & Interface Science **16**, 61 (2011).

[63] R. J. Rallison, Jour. Fluid Mech. **98**, 625 (1980).

[64] C. E. Chaffey and H. Brenner, J Colloid Interface Sci. **24**, 258 (1967).

[65] V. Sibillo, G. Pasquariello, M. Simeone, V. Cristini, and S. Guido, Phys. Rev. Lett. **97**, 054502 (2006).

[66] H. Xi and C. Duncan, Phys. Rev. E **59**, 3022 (1999).

[67] R. G. M. van der Sman and S. van der Graaf, Comput. Phys. Commun. **178**, 492 (2008).

[68] A. E. Komrakovaa, O. Shardt, D. Eskinb, and J. J. Derksen, International Journal of Multiphase Flow **59**, 23 (2014).

[69] H. Liu, A. J. Valocchi, and Q. Kang, Phys. Rev. E **85**, 046309 (2012).

[70] F. Magaletti, F. Picano, M. Chinappi, L. Marino, and C. M. Casciola, Jour. Fluid Mech. **714**, 95 (2013).

[71] M. Minale, Rheol. Acta **49**, 789 (2010).

[72] P. L. Maffettone and M. Minale, J. Non Newton. Fluid Mech **78**, 227 (1998).

[73] K. Verhulst, R. Cardinaels, P. Moldenaers, Y. Renardy, and S. Afkhami, J. Non-Newt. Fluid Mech. **156**, 29 (2009).

[74] K. Verhulst, R. Cardinaels, P. Moldenaers, S. Afkhami, and Y. Renardy, J. Non-Newt. Fluid Mech. **156**, 44 (2009).

[75] N. Aggarwal and K. Sarkar, J. Fluid Mech. **584**, 1 (2007).

[76] N. Aggarwal and K. Sarkar, J. Fluid Mech. **601**, 63 (2008).

[77] P. J. A. Janssen, A. Vananroye, P. V. Puyvelde, P. Moldenaers, and P. D. Anderson, J. Rheol. **54**, 1047 (2010).

[78] R. Cardinaels and P. Moldenaers, Microfluid Nanofluid **10**, 1153 (2011).

[79] P. E. Arratia, L.-A. Cramer, J. P. Gollub, and D. J. Durian, New J. Phys. **11**, 115006 (2009).

[80] L. Derzsi, M. Kasprzyk, J.-P. Plog, and P. Garstecki, Phys. Fluids **25**, 092001 (2013).